Global gyrokinetic ion temperature gradient turbulence simulations of ITER

2013 Plasma Phys. Control. Fusion 55 074017

(http://iopscience.iop.org/0741-3335/55/7/074017)

Plasma Phys. Control. Fusion **55** (2013) 074017 (8pp) doi:10.1088/0741-3335/55/7/074017

Global gyrokinetic ion temperature gradient turbulence simulations of ITER

L Villard[1], P Angelino[1], A Bottino[2], S Brunner[1], S Jolliet[1], B F McMillan[3], T M Tran[1] and T Vernay[1]

[1] Ecole Polytechnique Fédérale de Lausanne (EPFL), Centre de Recherches en Physique des Plasmas, Association Euratom-Switzerland, 1015 Lausanne, Switzerland
[2] Max-Planck Institut für Plasmaphysik, Association Euratom, Garching, Germany
[3] Centre for Fusion, Space and Astrophysics, University of Warwick, Warwick, UK

E-mail: laurent.villard@epfl.ch

Received 18 October 2012, in final form 13 November 2012
Published 14 June 2013
Online at stacks.iop.org/PPCF/55/074017

Abstract
Global gyrokinetic simulations of ion temperature gradient (ITG) driven turbulence in an ideal MHD ITER equilibrium plasma are performed with the ORB5 code. The noise control and field-aligned Fourier filtering procedures implemented in ORB5 are essential in obtaining numerically healthy results with a reasonable amount of computational effort: typical simulations require 10^9 grid points, 10^9 particles and, despite a particle per cell ratio of unity, achieve a signal to noise ratio larger than 50. As compared with a circular concentric configuration with otherwise similar parameters (same $\rho_* = 1/720$), the effective heat diffusivity is considerably reduced for the ITER MHD equilibrium. A self-organized radial structure appears, with long-lived zonal flows (ZF), modulating turbulence heat transport and resulting in a corrugated temperature gradient profile. The ratio of long-lived ZF to the fluctuating ZF is markedly higher for the ITER MHD equilibrium as compared with circular configurations, thereby producing a more effective ITG turbulence suppression, in spite of a higher linear growth rate. As a result, the nonlinear critical temperature gradient, $R/L_{T\mathrm{crit,NL}}$, is about twice the linear critical temperature gradient, $R/L_{T\mathrm{crit,lin}}$. Moreover, the heat transport stiffness above the nonlinear threshold is considerably reduced as compared with circular cases. Plasma elongation is probably one of the essential causes of this behaviour: indeed, undamped ZF residual levels and geodesic acoustic mode damping are both increasing with elongation. Other possible causes of the difference, such as magnetic shear profile effects, are also investigated.

(Some figures may appear in colour only in the online journal)

1. Introduction

First-principles based simulations of turbulence in magnetically confined plasmas have benefited over recent years from substantial progress [1] on theory and numerical algorithms, which made them particularly suitable for the high-end high performance computing (HPC) platforms available today. This has allowed us to include more and more physics in the codes and to consider fusion reactor real size systems such as ITER. Progress is being made also on the accurate description of realistic background magnetic geometry, which appears to have a significant effect on turbulent transport: for example, it was shown [2] that approximate geometrical models can lead to differences in the predicted heat diffusivity by a factor of 2 for a well-known benchmark case (Cyclone). The Cyclone base case (CBC) parameters [3] were inspired from a series of high confinement discharges in DIII-D that, incidentally, were aiming at finding out the effect of plasma shaping on confinement [4]. Whereas these experiments did evidence a positive effect of increasing elongation, it must be recalled that the CBC benchmark parameters were considering simple circular cross-section plasmas.

The CBC was also the starting point for series of simulations aiming at finding out finite size effects on ion temperature gradient (ITG) driven turbulence, the size parameter being defined as the ratio of ion sound Larmor

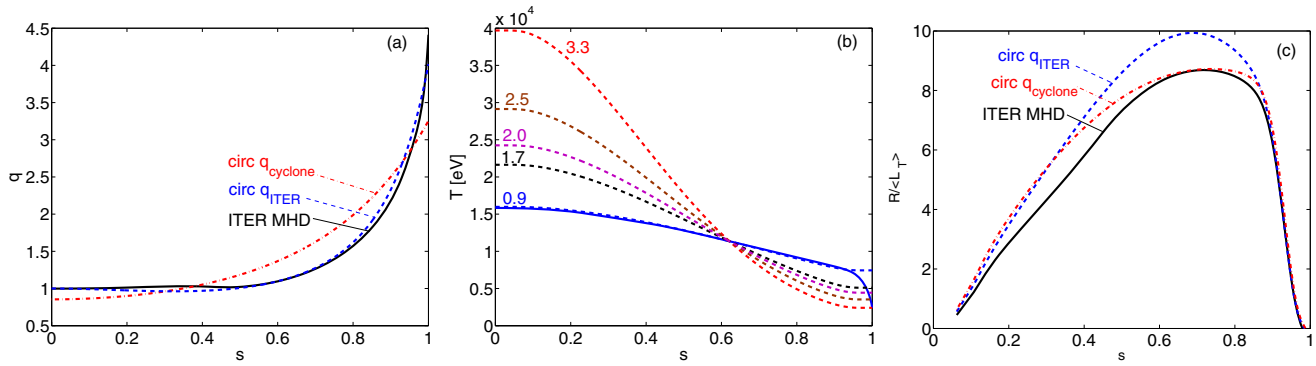

Figure 1. (*a*) q profiles for the three different configurations considered: ITER MHD, circular Cyclone, and circular with a q profile close to the ITER MHD case; (*b*) T profiles for various κ_T values labeling the respective curves, the solid line representing the T profile taken from an ITER inductive scenario simulation; and (*c*) $R/\langle L_T\rangle$ profiles for $\kappa_T = 2.484$.

radius to plasma minor radius $\rho_* = \rho_s/a$. These works served also as a benchmark comparison between different global gyrokinetic codes [5, 6] based on different numerical approaches and agreement could be demonstrated [7]. Finite ρ_* effects decrease the effective ion heat diffusivity by about 40% for the DIII-D/Cyclone size as compared with the infinite size result.

On the other hand, global gyrokinetic studies on the effects of plasma elongation were also performed in small size systems and showed a substantial reduction in turbulent transport [8]. The main reason for this is to be found in the zonal flow (ZF) dynamics [9]: plasma elongation increases the damping of the oscillatory component of the ZFs—the geodesic acoustic mode (GAM) [10]—and increases the undamped, zero frequency component—the Rosenbluth–Hinton residual [11]. Since steady ZFs are more effective than finite frequency ZFs in suppressing turbulence [12] through their shearing effect, the elongation has the overall effect of reducing turbulence-induced transport.

In this paper, we show the first global ITG turbulence simulation results of an ITER-size plasma having a magnetic configuration determined as an ideal MHD equilibrium consistent with one of the basic scenarios foreseen for its operation.

For the sake of comparing these ITER simulations with the CBC, we choose two intermediate cases: both have the circular geometry of CBC and the size of ITER, the first one has the same q profile as CBC whereas the other one uses the same q profile as the ITER ideal MHD equilibrium. The aim is to try to separate out the magnetic shear profile effects from the plasma shaping effects.

The rest of the paper is organized as follows: in the next section the physical model and numerical approach are briefly presented. Then, the ITER ideal MHD equilibrium is described and the choice of profile parameters introduced. The main results of turbulence simulations are presented in section 3, with scans in the ITG. Whereas linear results show a unfavourable effect of both the current profile and geometry of ITER (as compared with CBC), the *opposite* is true for nonlinear results: there is, notably, a much larger difference between the linear and nonlinear critical temperature gradients for the ITER configuration. Also, a much reduced profile stiffness is predicted. Conclusions are summarized in section 4.

2. Gyrokinetic equations and magnetic configuration

The ORB5 code [13] is a global gyrokinetic code using a PIC δf finite element representation, based on Hahm's equations [14]. It uses a straight-field-line coordinate system, and advanced noise control techniques such as a field-aligned Fourier filter, a ZF preserving Krook-like operator [15] and a coarse graining algorithm [16, 17]. It can include electromagnetic perturbations [18] and collision operators [19, 20], though in this paper collisionless electrostatic runs are performed.

The background magnetic equilibrium configuration is toroidal axisymmetric. It is obtained from the ideal MHD code CHEASE [21]. An inductive ITER scenario is considered here, with the main parameters $B_0 = 5.3\,\mathrm{T}$, $R_0 = 6.2\,\mathrm{m}$, $a = 2\,\mathrm{m}$, elongation $b/a = 1.88$, $I_\mathrm{p} = 15\,\mathrm{MA}$. The q profile is shown in figure 1(*a*). The cross-section is up–down asymmetric, and special care must be taken for particle boundary conditions at the plasma surface: when a marker leaves the surface, it is put back at the same ψ (poloidal flux), at a poloidal angle θ_* with the same B but the opposite sign of $\partial B/\partial\theta_*$ (figure 2), thus ensuring that the marker will reenter the plasma (otherwise markers are continuously lost for the simulation, which is detrimental for the signal/noise ratio), while at the same time ensuring conservation of particle energy, magnetic moment and toroidal canonical momentum $\psi_0 = \psi + (m/q)v_\parallel F(\psi)/B$, where $F(\psi) = RB_\varphi$ and φ is the toroidal angle. The temperature profiles are shown in figure 1(*b*), where the solid line is the result of a transport scenario simulation and the dashed lines show various cases considered for the gyrokinetic ORB5 simulations, for which the temperature gradient is parametrized as:

$$\frac{1}{T}\frac{\mathrm{d}T}{\mathrm{d}\tilde{\psi}} = -\kappa_T\Big(\tanh(s_1/2\rho_*) - \tanh(s_2/2\rho_*)\Big) \times\Big(1 - 1/\cosh^2(s_1/0.05) - 1/\cosh^2(s_2/0.05)\Big) \qquad (1)$$

with $s_1 = s - 0.025$, $s_2 = s - 0.975$, $s = \sqrt{\tilde{\psi}}$, $\tilde{\psi} = \psi/\psi_a$, ψ_a is the poloidal flux at the plasma boundary. It produces profiles

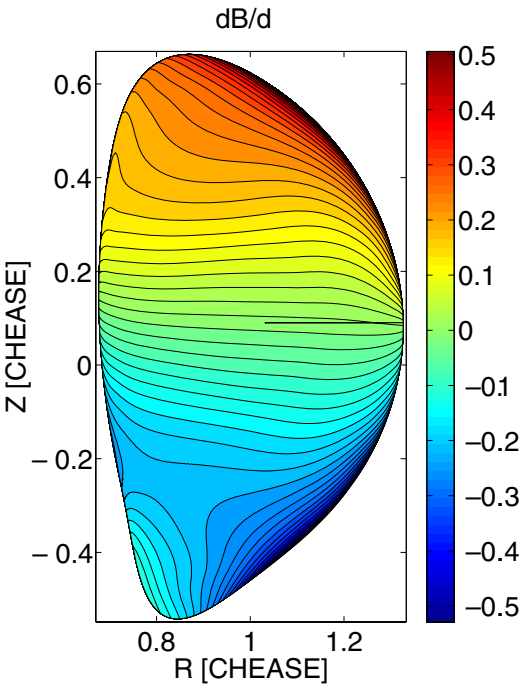

Figure 2. Contours of $\partial B/\partial\theta_*$ for the ITER ideal MHD equilibrium.

with $\mathrm{d}\ln T/\mathrm{d}\tilde{\psi} \approx \text{const} = -\kappa_T$ over most of the plasma radius ($s \in [0.2, 0.8]$). The normalized Larmor radius considered in all simulations is $\rho_* = 1/720$, which would correspond to $T_\mathrm{e} = 10.5\,\mathrm{keV}$ at mid-radius for a deuterium plasma. In order to ensure sufficient smoothness of the equilibrium coefficients, the plasma boundary considered in the simulations is taken at 98% of the separatrix flux. In this paper, we do not address the question of edge transport. As can be seen from figure 1(*b*) for $\kappa_T = 0.9$, the ORB5 parametrized profiles match the CHEASE profiles well for $s \leqslant 0.92$ but are markedly different beyond (the so-called pedestal). We chose $T_\mathrm{e}(s) = T_\mathrm{i}(s)$ for all cases shown in this paper. The density profile is parametrized in a similar way, with a coefficient κ_n such that $\eta_i = 3.1481$ is kept constant.

The CBC comparisons were until now performed on simplified circular cross-section magnetic configurations. We use here an approximation, i.e., not a true ideal MHD equilibrium, but keep all geometrical terms consistent, which was shown to be important in order to get quantitatively correct results [2]. The magnetic flux is chosen as circular concentric surfaces defined by $\mathrm{d}\psi/\mathrm{d}\rho = B_0\rho/\bar{q}(\rho)$, where $\rho = r/a$, with a specified $\bar{q}$ profile, resulting in $q = \bar{q}/\sqrt{1-\rho^2/R_0^2}$. Figure 1(*a*) shows the different q profiles used: the Cyclone q profile is defined by $\bar{q} = 0.854 + 2.184\rho^2$. In addition, we consider an intermediate case between Cyclone and ITER, i.e. a circular concentric configuration with $\bar{q} = 1 - 1.8\rho^2 + 4.55\rho^3$ resulting in a q profile matching closely that of the ideal MHD ITER equilibrium. We note that the most striking difference between the Cyclone and ITER q profiles is the larger q for $0.4 < s < 0.9$. (Note that $s = 0.62$ corresponds to mid-plasma radius $\rho_\mathrm{tor} = 0.5$, having defined $\rho_\mathrm{tor} = \sqrt{\Phi/\Phi_a}$, where Φ is the magnetic toroidal flux and Φ_a its edge value.)

For the same value of κ_T, different magnetic equilibria result in the same $T(s)$ profiles (and in particular the same $T_\mathrm{axis}/T_\mathrm{edge}$), but different profiles of the flux surface-averaged normalized logarithmic gradient

$$R/\langle L_T\rangle = R_0\frac{\mathrm{d}T/\mathrm{d}\psi}{\mathrm{d}V/\mathrm{d}\psi}S, \tag{2}$$

where S is the area of the flux surface and V is the volume enclosed by the flux surface. Figure 1(*c*) illustrates this for the case $\kappa_T = 2.484$. We also define a *global* normalized logarithmic gradient as

$$R/L_{T\,\mathrm{global}} = \frac{R_0}{a\rho_\mathrm{tor,ped}}\,\frac{T_\mathrm{axis}-T_\mathrm{ped}}{T_0}, \tag{3}$$

where T_0 is the temperature at mid-plasma radius, T_ped at the top of the pedestal, which we consider here at the normalized minor radius $\rho_\mathrm{tor,ped} = 0.9$,

Let f be the distribution function of a plasma species of mass m_s, charge q_s and ϕ the electrostatic potential. Let us define the following flux densities:

$$\Gamma = \int f\frac{\mathrm{d}\boldsymbol{R}}{\mathrm{d}t}\mathrm{d}^3v \tag{4}$$

$$\boldsymbol{q}_\mathrm{kin} = \int \frac{1}{2}m_s v^2 f\frac{\mathrm{d}\boldsymbol{R}}{\mathrm{d}t}\mathrm{d}^3v \tag{5}$$

$$\boldsymbol{q}_\mathrm{pot} = \int f q_\mathrm{i}\phi\frac{\mathrm{d}\boldsymbol{R}}{\mathrm{d}t}\mathrm{d}^3v \tag{6}$$

$$\boldsymbol{q}_\mathrm{H} = \boldsymbol{q}_\mathrm{kin} + \boldsymbol{q}_\mathrm{pot} - \frac{5}{2}m_s v_\mathrm{th}^2\Gamma. \tag{7}$$

We then define an 'effective' heat diffusivity χ_eff such that

$$\boldsymbol{q}_\mathrm{H} = -n\chi_\mathrm{eff}\nabla T \tag{8}$$

and assume that it is constant on a flux surface. Taking the flux-surface average, we obtain

$$\chi_\mathrm{eff} = -\frac{\langle\boldsymbol{q}_\mathrm{H}\cdot\nabla\psi\rangle}{n\,\mathrm{d}T/\mathrm{d}\psi\,\langle|\nabla\psi|^2\rangle}. \tag{9}$$

This definition is used throughout the paper. Numerically, the flux surface averaged fluxes are assembled from equidistant bins in ψ: $q_\mathrm{H,bin} = \int_\psi^{\psi+\Delta\psi}\int_0^{2\pi}\int_0^{2\pi}\boldsymbol{q}_\mathrm{H}\cdot\nabla\psi\,J_{\theta_*\psi\varphi}\,\mathrm{d}\psi\,\mathrm{d}\theta_*\,\mathrm{d}\varphi$, where $J_{\theta_*\psi\varphi} = qR^2/F$ is the Jacobian of the straight-field-line coordinate system $(\theta_*, \psi, \varphi)$. Thus,

$$\chi_\mathrm{eff} \approx -\frac{q_\mathrm{H,bin}}{n\Delta T_\mathrm{bin}\int_0^{2\pi}\int_0^{2\pi}|\nabla\psi|^2 J_{\theta_*\psi\varphi}\,\mathrm{d}\psi\,\mathrm{d}\theta_*\,\mathrm{d}\varphi}. \tag{10}$$

The gyro-Bohm unit for the diffusivity is defined as $\chi_\mathrm{GB0} = \rho_\mathrm{s0}^2 c_\mathrm{s0}/a$, with a the minor radius on the equatorial plane, ρ_s0 the ion sound Larmor radius and c_s0 the ion sound speed with the temperature taken at mid-radius and the magnetic field on axis. For the parameters considered in this paper, $\chi_\mathrm{GB0} = 2.75\,\mathrm{m^2\,s^{-1}}$.

To characterize the ZF profiles, we define the flux-surface-averaged potential

$$\langle\phi\rangle(s,t) = \frac{\int\phi J_{\theta_*\psi\varphi}\,\mathrm{d}\theta_*\,\mathrm{d}\varphi}{\int J_{\theta_*\psi\varphi}\,\mathrm{d}\theta_*\,\mathrm{d}\varphi}, \tag{11}$$

an effective $E \times B$ ZF velocity

$$v_{E\times B}(s,t) = \frac{1}{aB_0}\frac{\partial\langle\phi\rangle}{\partial s} \tag{12}$$

and an effective $E \times B$ ZF shearing rate [23]

$$\omega_{E\times B}(s,t) = \frac{s}{2\psi_a q}\frac{\partial}{\partial s}\left(\frac{1}{s}\frac{\partial\langle\phi\rangle}{\partial s}\right). \tag{13}$$

The gyro-Bohm units for $v_{E\times B}$ and $\omega_{E\times B}$ are c_{s0} and c_{s0}/a, respectively.

3. Simulation results: from Cyclone to ITER

The following numerical parameters are chosen: unless specified otherwise, the number of markers is $N_p = 10^9$, the 3D grid for the field solver is $N_s \times N_{\theta_*} \times N_\varphi = 512 \times 2048 \times 1024$. Note that we have 10^9 grid points, resulting in 1 particle/cell on average. This would be clearly very low if no field-aligned Fourier filter were applied to the perturbed density: here, we keep poloidal modes $m \in [nq - \Delta m, nq + \Delta m]$, with $\Delta m = 9$: we eliminate modes with parallel wavenumbers larger than $k_\parallel^{\max} = B_\varphi \Delta m / BRq$, consistent with gyrokinetic ordering [13]. Moreover, we solve in a toroidal wedge of 1/8 of the full torus, which translates in Fourier space as having only multiples of 8 as toroidal mode numbers. We truncate the Fourier mode numbers at $n_{\max} = 384$. Thus, the number of radial intervals and Fourier modes retained in our simulations is $N_s(2\Delta m + 1)(n_{\max}/8 + 1) = 476\,672$, resulting in an average number of particles per mode of more than 2000 for $N_p = 10^9$, ensuring a sufficiently high signal/noise ratio: for all simulations presented in this paper, $S/N > 50$. For more details on the S/N estimate see [22]. Noise is controlled on long time scales using a Krook operator as described in [15] with a decay rate $\gamma_K = 1.752 \times 10^{-5}\Omega_i = 0.0126 c_{s0}/a$ and enforced conservation of ZF residual, particle density and parallel flow. Conservation of energy is not enforced, so this operator acts to relax the temperature profile towards the specified initial profile, maintaining the radial and time-average temperature gradients roughly constant on long time scales: our simulations are thus 'gradient-driven', though short variations are allowed, as will be seen in the results presented below. The time step is $\Delta t = 160\Omega_i^{-1} = 0.2222 a/c_{s0}$. The choice of numerical parameters was put to test, among other things by performing simulations in a toroidal wedge of 1/16 of the full torus or $n_{\max} = 256$ or $\Delta m = 5$ or $\Delta t = 80\Omega_i^{-1}$ or $\gamma_K = 0.876 \times 10^{-5}\Omega_i$ or $N_p = 2 \times 10^9$ and showed no significant difference in the physical results.

In the frame of the HP2C project the ORB5 code has been further optimized in view of its application to large system sizes requiring large grid numbers such as these. Reorganization of the global communications has resulted in a factor of 2 improvement in wall clock time. The simulations in this paper require 13 s/timestep on 4096 cores of the HELIOS supercomputer. Typically, 7500 timesteps are necessary in order to reach a satisfactory quasi-steady state, thus a full simulation costs about 100 000 core-hours. In gyro-Bohm units the simulation time is about $1700 a/c_s$.

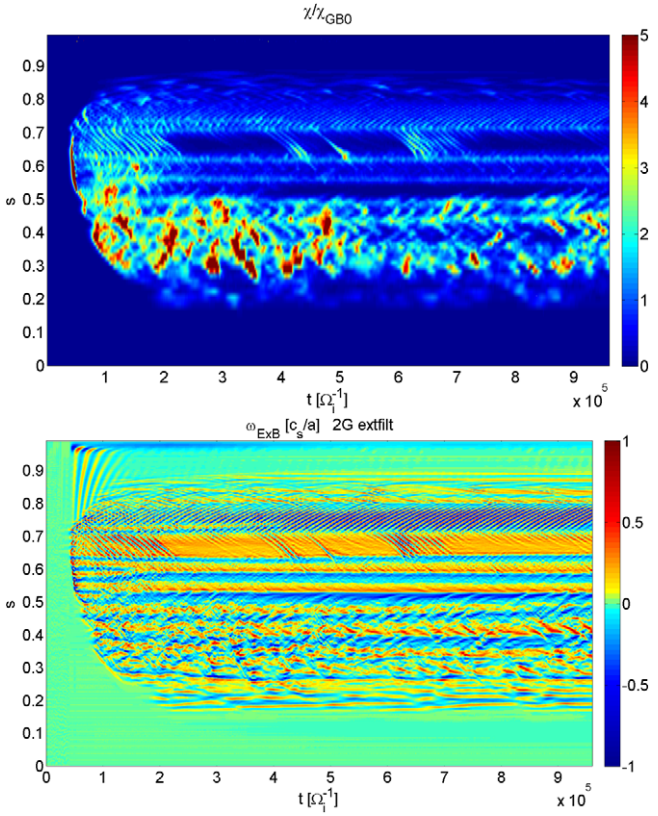

Figure 3. Contours of effective ion heat diffusivity χ_{eff} (top) and ZF shearing rate $\omega_{E\times B}$ (bottom) versus radial coordinate s and time, for the ITER MHD case with $\kappa_T = 3.3$ ($R/L_{T\,\text{global}} = 11.25$).

A global gyrokinetic simulation with $\kappa_T = 3.3$ ($R/L_{T\,\text{global}} = 11.25$) with $N_p = 2 \times 10^{19}$ particles is performed in the ITER ideal MHD equilibrium. Figure 3 (top) shows the contours of χ_{eff} versus radius s and time. After an initial turbulence overshoot starting near $s \sim 0.6$–0.7, which is in the region of maximum $R/\langle L_T\rangle$, several bursts (localized features in space and time) and avalanches (observed as oblique features on the figure) occur intermittently, propagating inwards or outwards. Note that the heat flux associated with an avalanche is always outwards, irrespective of the direction of propagation of the avalanche. In addition, long-lived radial structures appear as modulations of the time-average heat transport.

Figure 3 (bottom) shows contours of the $E \times B$ ZF shearing rate $\omega_{E\times B}(s,t)$. Clearly, the long-lived structures and avalanches of $\omega_{E\times B}$ and of χ_{eff} are correlated. Around $s \sim 0.75$, avalanches occur with remarkable regularity: as a matter of fact, a rather well-defined frequency can be measured, so this appears as a quasi-coherent mode. The frequency is about equal to half the GAM frequency at that radius. This might suggest some form of parametric decay instability. It should be noted that the direction of propagation of avalanches is outwards in regions of negative time-averaged ZF shearing rate, and inwards in regions of positive time-averaged ZF shearing rate. This is consistent with the findings of [24], where background flows were considered; thus, in our simulations the long-lived ZF structures play the same role as background flows in deciding on the avalanche direction

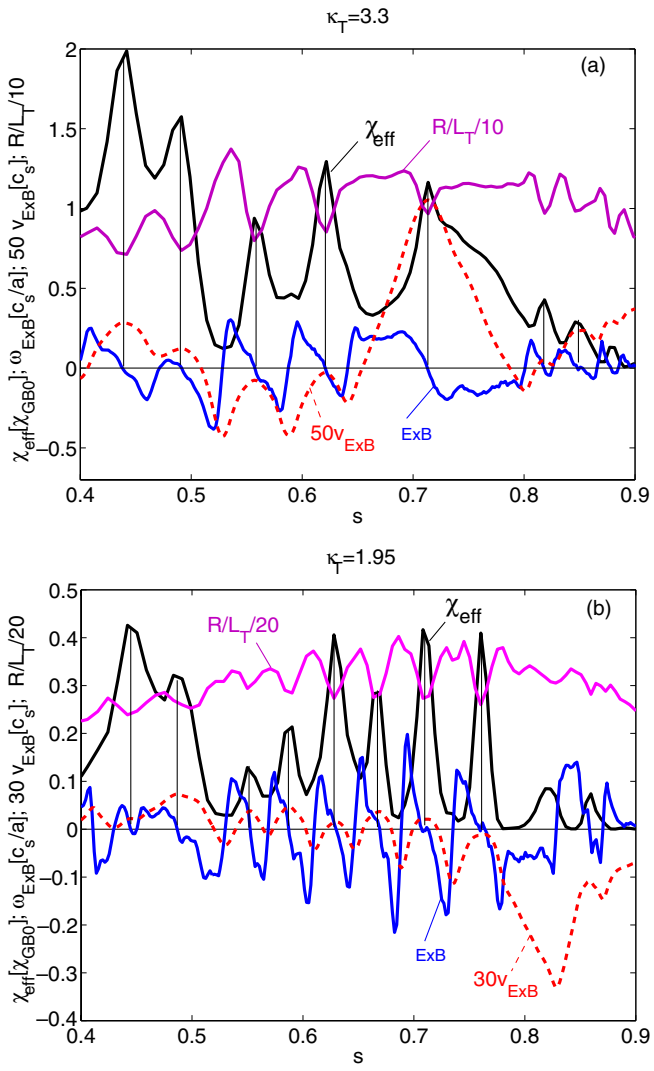

Figure 4. Radial profiles of effective ion heat diffusivity $\chi_{\rm eff}$, ZF shearing rate $\omega_{E\times B}$, ZF velocity $v_{E\times B}$ and flux-surface-averaged logarithmic temperature gradient $R/\langle L_T\rangle$. The quantities are time-averaged over the last half of the simulation and are rescaled in order to make them visible on the same plot. The thin vertical lines are drawn to underline the correspondance between local maxima of $\chi_{\rm eff}$, minima of $R/\langle L_T\rangle$, maxima of $v_{E\times B}$ and zeros of $\omega_{E\times B}$. ITER MHD configuration, (*a*) for $\kappa_T = 3.3$ ($R/L_{T\ \rm global} = 11.25$); (*b*) for $\kappa_T = 1.95$ ($R/L_{T\ \rm global} = 5.81$).

of propagation, a feature already observed in [25]. Another feature is prominent: at the time of the early turbulence overshoot, a strong GAM is excited, propagating outwards and being quickly damped. These observations are consistent with the findings of [9], which in particular showed a strongly enhanced GAM damping due to plasma elongation.

Taking a closer look at the relationship between ZFs and turbulent transport, we show in figure 4(*a*) the radial profiles of *time-averaged* ZF shearing rate, ZF velocity, effective heat diffusivity and flux-surface-averaged normalized logarithmic temperature gradient (some quantities are rescaled so that they all appear on the same plot). Local maxima of $\chi_{\rm eff}$ correspond accurately and systematically to zero ZF shearing rate positions. This is consistent with the picture of turbulence suppression by sheared flows. A closer inspection shows that this happens only at *maxima* positions of the ZF velocity, the minima positions of ZF velocity corresponding in fact to minima in $\chi_{\rm eff}$. (Note that maxima in $v_{E\times B}$ mean minima in radial ZF electric field, due to our definition in equation (12).) For $s \lesssim 0.65$, the ZF velocity profile assumes the shape of linked parabolas of negative curvature and thus the ZF shearing rate has a sawtooth-like radial profile. Thus, in the vicinity of *minima* of ZF velocity the absolute value of the ZF shearing rate is large and turbulence is suppressed, once again consistent with the turbulence-sheared flow picture. Around $s = 0.72$ the $v_{E\times B}$ profile is more V-shaped. Expectedly, maxima positions of $\chi_{\rm eff}$ correspond to minima in temperature gradient profile, the enhanced transport in these positions resulting in a local temperature flattening. Another feature is worth mentioning: the avalanches are triggered at positions of zero ZF shearing rate and maximum $v_{E\times B}$ (i.e. minimum ZF radial electric field), which correspond to *local minima* in temperature gradient: a similar finding is reported in [26]. The triggering of avalanches is particularly visible around $s = 0.72$: figure 3 (bottom) shows that avalanches start there and propagate either outwards, in the radial zone $0.72 < s < 0.8$, or inwards, in the zone $0.63 < s < 0.72$. The time-averaged results of figure 4(*a*) show that the ZF shearing rate is positive in the zone $0.72 < s < 0.8$ and negative in the zone $0.63 < s < 0.72$, and the ZF velocity has indeed a local maximum at $s = 0.72$. It is difficult at this point to determine a causality relation between the triggering position of avalanches and the long-lived ZF structure; we merely note that the direction of propagation of avalanches is determined by the sign of the time-averaged ZF shearing rate, consistent with [24].

We have performed a series of simulations with varying values of κ_T. For $\kappa_T = 1.95$ ($R/L_{T\ \rm global} = 5.81$), the time-averaged profiles of $\chi_{\rm eff}, \omega_{E\times B}, v_{E\times B}$ and $R/\langle L_T\rangle$ are shown in figure 4(*b*). The same qualitative conclusions can be drawn, in particular on the relationship between long-lived ZF structures and heat transport. Quantitatively, the system is close to having completely quenched turbulence, and avalanches and bursts are less frequent.

In order to compare with CBC, we have performed similar gradient scans for circular configurations with the same normalized plasma size $1/\rho_* = 720$ and the same temperature gradient parametrization (equation (1)), one with the original CBC q profile, the other with a q profile closely matching that of the ITER ideal MHD equilibrium (figure 1(*a*)). The main results of our investigations are reported in figure 5, showing in continuous lines the effective heat diffusivity $\chi_{\rm eff}$ (radially averaged ($s \in [.4.8]$), time-averaged over the last half of the simulations) as a function of the normalized global logarithmic temperature gradient $R/L_{T\ \rm global}$. Curves with black squares are for the ITER MHD equilibrium, curves with open circles for the CBC case, curves with '+' for the circular case with ITER-like q profile. In this figure, we plot also in dashed lines the linear growth rates for ITG modes with $k_\theta \rho_{\rm s} \approx 0.5$ at mid-radius. First, we note that going from a circular to an ITER-shaped plasma is *linearly destabilizing* for small gradients, resulting in a smaller critical gradient, and linearly stabilizing for large gradients. Second,

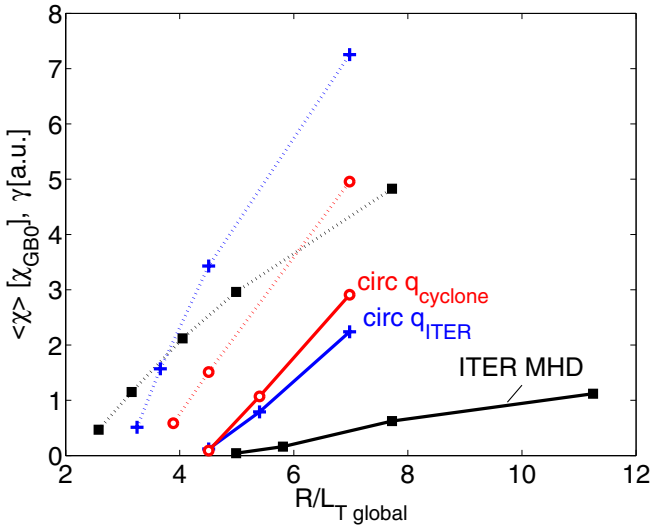

Figure 5. Solid lines: effective turbulent ion heat diffusivity $\chi_{\rm eff}$, radially averaged $s \in [0.4, 0.8]$; dashed lines: linear ITG growth rate γ for $k_\theta \rho_{\rm s} \approx 0.5$, as a function of the global normalized logarithmic temperature gradient $R/L_{T\ \rm global}$. Curves with black squares are for the ITER MHD equilibrium, curves with open circles for the circular Cyclone case, curves with '+' for the circular case with ITER-like q profile. All simulations performed with $1/\rho_* = 720$. The value of the gyro-Bohm normalization unit of diffusivity is $\chi_{\rm GB0} = 2.75\,{\rm m}^2\,{\rm s}^{-1}$ for ITER parameters.

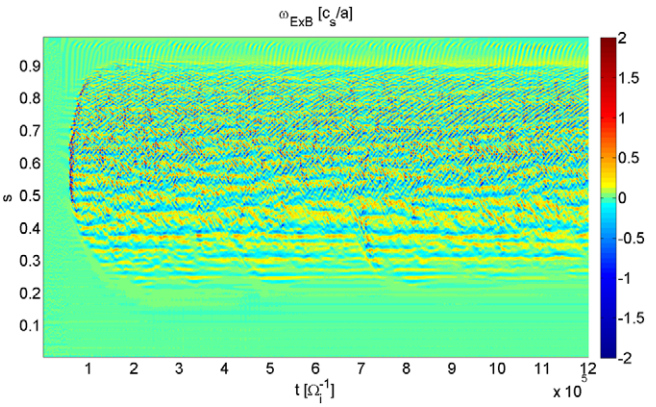

Figure 6. Contours of ZF shearing rate versus radius (s) and time, for the circular Cyclone case with $\kappa_T = 2.484$ ($R/L_{T\ \rm global} = 6.98$).

going from the Cyclone q profile to the ITER q profile is linearly destabilizing for all values of the temperature gradient. Second, the most remarkable feature of *nonlinear* simulation results is the dramatic *reduction* in heat transport when going from circular to ITER-shaped plasmas. The nonlinear critical temperature gradient, $R/L_{T{\rm crit,NL}}$, is about twice the linear critical temperature gradient, $R/L_{T{\rm crit,lin}}$. Moreover, the heat transport stiffness, i.e. the increase of effective heat diffusivity above $R/L_{T{\rm crit,NL}}$, is considerably reduced as compared with circular cases.

The main cause of the difference between circular cross-section and ITER-shaped equilibrium plasmas is to be found in the ZF behaviour: we show in figure 6 the contours of the ZF shearing rate versus radius and time for the circular Cyclone case with $\kappa_T = 2.484$ ($R/L_{T\ \rm global} = 6.98$). Comparing with the results of ITER plasma (figure 3, bottom), the most

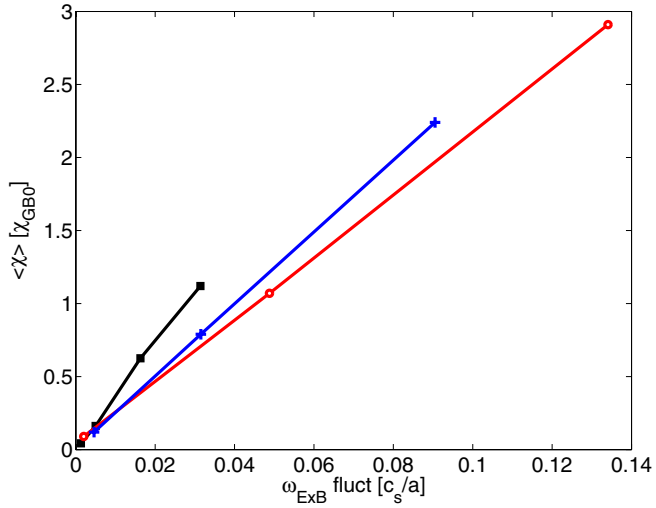

Figure 7. Effective turbulent ion heat diffusivity versus fluctuating component of the ZF shearing rate. Curves with black squares are for the ITER MHD equilibrium, curves with open circles for the CBC case, curves with '+' for the circular case with ITER-like q profile.

striking difference lies in the much less prominent quasi-steady state structures for the circular case. In order to quantify this behaviour, we define two quantities:

$$\omega^{\rm tot}_{E\times B} = \langle\langle|\omega_{E\times B}|\rangle_s\rangle_t \tag{14}$$

$$\omega^{\rm steady}_{E\times B} = \langle|\langle\omega_{E\times B}\rangle_t|\rangle_s \tag{15}$$

where the subscripts s and t indicate averages over radius ($s \in [.4\ .8]$) and time (the last half of the simulation), respectively. The first quantity is a measure of the total absolute value of the ZF shearing rate activity, while the second quantity is a measure of the quasi-steady ZF shearing rate. One can then define $\omega^{\rm fluct}_{E\times B} = \omega^{\rm tot}_{E\times B} - \omega^{\rm steady}_{E\times B}$ as a measure of the fluctuating part of the ZF shearing rate (due to avalanches, bursts and GAMs). It appears that the main difference between ITER-shaped and circular cases is the ratio of the fluctuating to the steady ZF sharing rates, that ratio being much larger for the ITER-shaped cases. An almost linear proportionality can be seen between the fluctuating part of the ZF shearing rate and the turbulent ion heat diffusivity, as clearly shown in figure 7. This can be understood as follows: below the upshifted critical gradient the ZFs are strong enough to completely suppress turbulence and thus the system ends in a state with no turbulent transport and purely steady ZFs. For gradients above this value, the ZF shearing rate cannot be sustained at large enough values to completely suppress turbulence, because they become Kelvin–Helmholz unstable [20]. As a consequence they cannot stay purely constant in time, i.e. a fluctuating part appears. Therefore, the turbulent transport is correlated with the fluctuating part of the ZFs.

Comparing the ZF spatio-temporal structures for the ITER and circular cases, figures 3 (bottom) and 6, respectively, another feature emerges: for the circular case, regular ZF oscillations are observed near the edge ($0.8 < s < 1$) throughout the simulation time. We have verified that these

oscillations do have a local frequency in very good agreement with the dispersion relation for GAMs given by equations (49) and (50) of [9]. Except for the initial transient GAM event discussed above, this feature is absent from the ITER simulation. Thus, GAMs are less easily excited by ITG turbulence in elongated plasmas than in circular plasmas.

Considering now the circular plasma with a q profile close to the ITER equilibrium, we can observe in figure 5, in spite of larger linear growth rates (dotted line with '+') than for the circular Cyclone case (dotted line with open circles), a very similar, even slightly reduced turbulent ion heat transport (solid lines with '+' and circles, respectively). The larger linear growth rates might be attributed to larger peak values of the flux-surface-averaged gradient, figure 1(c). On the other hand, the larger difference between linear and nonlinear thresholds is an indication of a more effective ZF shear stabilization. In fact, larger fractions of long-lived sheared ZF structures are seen, as compared with the Cyclone case. Also, GAM oscillations (except near the very edge $s > 0.95$) have a lower amplitude than for the Cyclone case. This is consistent with a stronger GAM damping due to a lower q over most of the plasma cross-section ($s < 0.95$), figure 1(a).

4. Conclusion

The main result of this paper is represented in figure 5: plasma shaping and, to a lesser extent, q profile variations have major repercussions on the turbulent ion heat flux. The implications are very favourable for ITER, with an increase in critical gradient and a drastically reduced profile stiffness. Summing up the results for the three configurations studied, a picture emerges whereby long-lived sheared ZF favours turbulence suppression, whereas the fluctuating part of the sheared ZF is clearly correlated with the turbulent heat transport (figure 7). Moreover, we have shown remarkable examples of turbulent self-organization, with the creation of long-lived parabolic or V-shaped ZF velocity structures (figure 4). One important result from these studies is that linear (or quasi-linear) estimates of turbulent transport would lead to not only quantitatively different results, but also *qualitatively* opposite conclusions from those resulting from a proper nonlinear analysis.

Elongation is tentatively the most important geometrical parameter favourizing turbulence suppression, as found in [8] using ideal MHD equilibria and in [27] using Miller's local equilibrium model [28]. However, the effects of other geometrical parameters should be separately investigated, e.g. plasma triangularity, up–down asymmetry and Shafranov shift [29]. This may provide the fusion research community with tools to optimize plasma confinement through plasma shaping.

This rather optimistic finding for ITER should not be considered as the final answer to the question of turbulent transport in that device. Several physical effects, not considered in this paper, may change the picture. First, the presence of a trapped electron population reduces the adiabatic response to only the passing electron population, which is known to increase the ITG linear growth rates. Moreover, trapped electron modes (TEM) could be destabilized, in particular once ITGs are stabilized by ZF. First nonlinear TEM results in circular plasmas at low $1/\rho_*$ [30, 31] indicate that TEMs are less effectively suppressed by ZF shearing than ITG. Second, ion–ion collisions are known to damp the ZF, resulting in nonzero turbulent transport in the 'Dimits shift' region [20]. It is unclear whether the long-lived ZF structures will survive in a collisional turbulent simulation [26, 32]. In this context, the question of parallel momentum transport should also be investigated. Third, the heat source considered in this paper is not realistic. Although the avalanches seem qualitatively independent of whether the simulations are gradient-driven or flux-driven [33], it should be verified in flux-driven simulations [25, 26, 34] whether the 'corrugated' transport pattern [35] subsists on long time scales and, more importantly, if the observed reduction in ion heat transport through plasma elongation is confirmed. Fourth, the non-adiabatic electron response localized in the vicinity of mode-rational surfaces [36] might have an influence on the radial structures. Fifth, finite β effects, e.g. through the equilibrium Shafranov shift, are known to stabilize ITG modes. Future investigations should consider ideal MHD equilibria consistent with the plasma profiles used for turbulence studies. Finally, the question of turbulent transport in the edge pedestal region, which was not addressed in this paper, should be considered.

Acknowledgments

This work was partly supported by the Swiss National Science Foundation, by the HP2C project, and by the European Communities within the framework of the European Fusion Development Agreement. Simulations were performed on the IFERC-CSC HELIOS platform, mainly under the Lighthouse Project, and on the CSCS ROSA platform. The authors thank Dr O Sauter for providing the ITER equilibrium input.

References

[1] Garbet X, Idomura Y, Villard L and Watanabe T H 2010 *Nucl. Fusion* **50** 043002
[2] Lapillonne X *et al* 2009 *Phys. Plasmas* **16** 032308
[3] Dimits A M *et al* 2000 *Phys. Plasmas* **7** 969
[4] Greenfield C M *et al* 1997 *Nucl. Fusion* **37** 1215
[5] Lin Z, Ethier S, Hahm T S and Tang W M 2002 *Phys. Rev. Lett.* **88** 195004
[6] Candy J, Waltz R E and Dorland W 2004 *Phys. Plasmas* **11** L25
[7] McMillan B F *et al* 2010 *Phys. Rev. Lett* **105** 155001
[8] Angelino P *et al* 2009 *Phys. Rev. Lett* **102** 195002
[9] Angelino P *et al* 2008 *Phys. Plasmas* **15** 062306
[10] Winsor N *et al* 1968 *Phys. Fluids* **11** 2448
[11] Rosenbluth M N and Hinton F L 1998 *Phys. Rev. Lett.* **80** 724
[12] Hahm T S *et al* 1999 *Phys. Plasmas* **6** 922
[13] Jolliet S *et al* 2007 *Comput. Phys.Commun.* **177** 409
[14] Hahm T S 1988 *Phys. Fluids* **31** 2670
[15] McMillan B F *et al* 2008 *Phys. Plasmas* **15** 052308
[16] Brunner S *et al* 1999 *Phys. Plasmas* **12** 4504
[17] Chen Y and Parker S E 2007 *Phys. Plasmas* **14** 082301
[18] Bottino A *et al* 2011 *Plasma Phys. Control. Fusion* **53** 124027
[19] Vernay T *et al* 2010 *Phys. Plasmas* **17** 122301
[20] Vernay T *et al* 2012 *Phys. Plasmas* **19** 042301

[21] Lütjens H, Bondeson A and Sauter O 2006 *Comput. Phys. Commun.* **97** 219
[22] Bottino A *et al* 2007 *Phys. Plasmas* **14** 010701
[23] Villard L *et al* 2002 *Phys. Plasmas* **9** 2684
[24] McMillan B F *et al* 2011 *Phys. Plasmas* **18** 112503
[25] Idomura Y. *et al* 2009 *Nucl. Fusion* **49** 065029
[26] Jolliet S and Idomura Y 2012 *Nucl. Fusion* **52** 023026
[27] Kinsey J E *et al* 2007 *Phys. Plasmas* **14** 102306
[28] Miller R L *et al* 1998 *Phys. Plasmas* **5** 973
[29] Burckel A *et al* 2010 *J. Phys.: Conf. Ser.* **260** 012006
[30] Jolliet S 2009 *PhD Thesis* No 4326 Ecole Polytechnique Fédérale de Lausanne
[31] Vernay T *et al* 2012 *Plasma Phys. Control. Fusion* **55** 074016
[32] Dif-Pradalier G *et al* 2009 *Phys. Rev. Lett.* **103** 065002
[33] Görler T *et al* 2011 *Phys. Plasmas* **18** 056103
[34] Sarazin Y *et al* 2010 *Nucl. Fusion* **50** 054004
[35] Dif-Pradalier G *et al* 2010 *Phys. Rev.* E **82** 025401
[36] Villard L *et al* 2010 *Plasma Phys. Control. Fusion* **52** 124038